Modeling and Simulation of High-Frequency Solar Irradiance

Wenqi Zhang, William Kleiber, Anthony R. Florita, Bri-Mathias Hodge, and Barry Mather

Abstract—As the use of solar power as a source of electricity is increasing, so is the interest in modeling radiation at high temporal resolutions. High-dimensional remote sensing data products depend on cloud cover variability, atmosphere aerosol levels, and other atmospheric parameters. Because of weather fronts and aerosols, it is difficult to quantify solar power variability based on distributed solar networks. The global horizontal irradiance (GHI) component in the National Solar Radiation Database (NSRDB) is available at a 30-min time resolution. The algorithm proposed in this paper produces 1-min-resolution GHI samples at locations where NSRDB data are available. The synthetic irradiance datasets are produced using log-additive non-Gaussian mixture models and resampling techniques. The model is trained over historical data, and predicted values are compared with *in situ* data. This approach allows for estimating the solar irradiance at subhourly temporal resolutions, while featuring variability for locations where measurements are otherwise not available.

Index Terms—Downscaling, irradiance generation, mixture distribution, stochastic modeling.

I. INTRODUCTION

THE design of new energy systems must account for the increasing use of renewable energy sources and their associated variability. The Renewable Global Status Report [1] shows that in 2015, more than 15% of total electricity was generated from renewable energy in 2015. Solar photovoltaic (PV) capacity was relatively small among all the renewables; however, solar power was cited as the most installed power source based on capacity in the United States during 2016 [1]. PV power is intermittent and variable, which, in turn, affects the stability of the system and the balance of electric power, increasing power compensation [2].

As higher levels of PV are integrated into the distribution system, the need for more accurate interconnection study methods (i.e., studies that determine the technical impacts of additional PV integration) is becoming increasingly important. Studies using quasi-static time-series analysis are becoming more prevalent and useful [3]. To gain the full benefit of these studies, accurate models of high-frequency solar irradiance at a temporal and spatial scale appropriate for distribution systems are required. Past work shows that the variability of integrated PV is more critical to understanding distribution system operations than the variability in loads [4]. Additionally, previous work on distribution-scale solar irradiance modeling used cloud-motion vector approaches [5] that showed significant improvement requires considerable input data and heavy computation.

Accurate PV power modeling not only plays an important role to ensure that the integrated power on smart grid is economically feasible, but also contributes to improvements in electric power quality and thus reduces price volatility [6]. Because PV power output is directly related to solar irradiance at the ground level, solar irradiance modeling is vital to the smart grid [7]; however, solar irradiance modeling is complicated by weather fronts and atmospheric conditions, such as wind speed, temperature, and relative humidity. Uncertainty related to natural weather conditions at the site level is inherent [8].

During the past few years, many solar irradiance forecasting models have been developed. These approaches can be broadly classified into three categories: statistical, machine learning, and physical. Statistical models such as autoregressive moving average and autoregressive integrated moving average have been widely applied on several occasions [9]–[11]. Another popular statistical approach is to use spatiotemporal models. Compared to others, spatiotemporal models have tremendous capability to approximate solar irradiance variability across time and space. Glasbey *et al.* [12] proposed a separable spatiotemporal model for solar data at 22 locations in Edinburgh, U.K. The semiparametric spatiotemporal model proposed in [12] is a functional coefficient autoregressive model. Machine-learning approaches such as artificial neural networks and support vector machines have been well established in recent years [13]–[16]. Physical models such as numerical weather prediction (NWP) models in conjunction with a sky imager are popular [17]. Lorenz *et al.* [18] showed that NWP is the most accurate technique for solar irradiance forecasts at a day-ahead prediction horizon. Techniques such as Kalman filters [19] and Bayesian model averaging [20] have been implemented

TABLE I
DATA USED TO TRAIN THE MODEL

Locations with available series	Time span
Eugene, OR	01/01/2013 to 12/31/2013
Portland, OR	01/01/2013 to 12/31/2013
Salem, OR	01/01/2013 to 12/31/2013

All radiation measurements are in W/m^2.
Source: National Renewable Energy Laboratory.

to improve NWP irradiance predictions; however, cloud cover solar forecasting remains unresolved using NWP.

The focus of this work is on solar resource assessment and solar irradiance variability estimation. Several approaches to synthetically generate irradiance time series for an individual site have been proposed in recent years. Hummon *et al.* [21] converted all irradiance values to the clearness index and synthesized them based on five classifications of cloud cover. A wavelet-based model was used in [22]. In [23], a Markov model was introduced to generate 1-min global solar radiation data based on mean hourly meteorological observations. Spatial variation was added in [24], improving the model's geographical flexibility. Other authors have examined spatial variation of irradiance [25]–[27]. Perez and Fthenakis [27] used cloud motion to study the spatial anisotropic nature of solar irradiance. There are other methods in the literature [28]–[30]. In this proposed work, a jump process allows for additional spikes based on the presence of different cloud types to capture scattering events. The first part of the model is a decision rule to distinguish between clear and non-clear days. Furthermore, the method depends only on the National Solar Radiation Database (NSRDB) [31].

The proposed method is trained on a set of sample locations in Oregon and then validated at seven locations across the United States. Overall, the downscaled ensembles capture variability properly. The rest of this paper is structured as follows. Section II introduces the database used in this work. Section III describes the methodology proposed for generating stochastic 1-min global horizontal irradiance (GHI) data based on the NSRDB. Section IV shows various validation metrics. Section V includes conclusions and future work.

II. DATA

The model is trained based on three locations from the Pacific Northwest (see Table I). The satellite data used in this work are from the NSRDB, which contain gridded satellite estimates of solar radiation at a 30-min time resolution and at an approximate spatial resolution of 4 km by 4 km [31]. The database spans the entire United States, but only Oregon data are used to train the model. These series run from January 1, 2013, to December 31, 2013, and comprise 17 520 observations for each location. The measure of irradiance is the global horizontal component, in W/m^2. The ground measurement is at a resolution of 1 min from the Solar Radiation Monitoring Laboratory, University of Oregon [33]. The ground measurements are within a 16-km^2 grid of the laboratory site. Fig. 1 illustrates the relationship between linear interpolated NSRDB
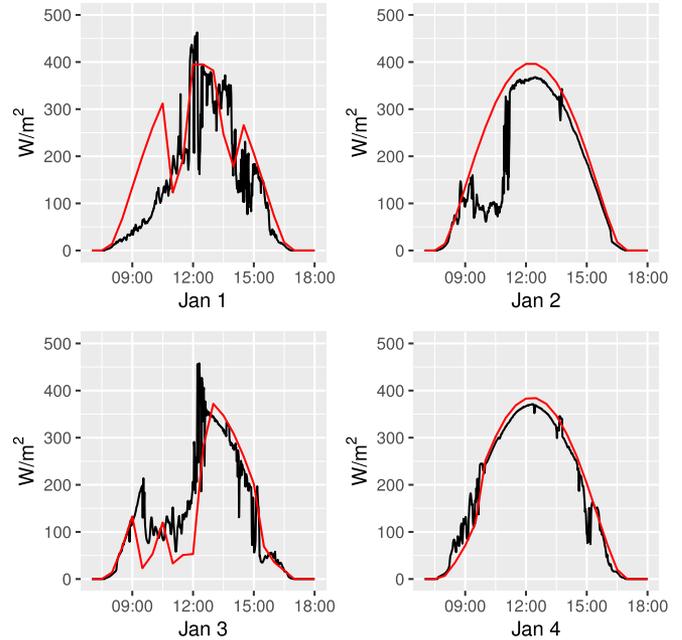

Fig. 1. Linearly interpolated NSRDB data at 1-min resolution (red) and *in situ* data (black) for Eugene, OR, USA, January 1–4, 2013.

TABLE II
MODEL VALIDATION LOCATIONS

Site	Climate
Bondville, IL	Humid continental
Boulder, CO	Semi-arid
Desert Rock, NV	Desert
Fort Peck, MT	Semi-arid
Goodwin Creek, MS	Humid subtropical
Penn State University, PA	Humid subtropical
Sioux Falls, SD	Humid subtropical

All radiation measurements are in W/m^2.
Source: National Oceanic and Atmospheric Administration.

data and *in situ* measurements at Eugene, OR, USA, for January 1–4, 2013. Even though the satellite data follow the general trend of the *in situ* measurements, there is substantial high-frequency variability in the *in situ* measurements that is not captured in the satellite-based product, e.g., January 2, as shown in Fig. 1.

The NSRDB data include cloud cover type, and GHI is divided into two indices: estimates of actual GHI and clear-sky GHI. The latter is an estimate of maximal possible GHI given clear atmospheric conditions. Clear-sky indices are derived from the Reference Evaluation of Solar Transmittance 2 model [32]. Values represent theoretical maximum GHI at any site where sun photometric data are available.

The validation locations shown in Table II are from the Surface Radiation Budget Network (SURFRAD), which is a network of observation stations across the United States with high-quality *in situ* data at a 1-min resolution [34].

III. STOCHASTIC DOWNSCALING

The first part of the chosen approach is an initial decision tree to determine what type of day to simulate. Intuitively, there should be little deviation from the clear-sky index on a clear day. Thus, clear days are modeled separately using linear interpolated clear-sky GHI. Instead of the complicated algorithm proposed in [35] to identify clear periods for each day, a simple clear-day decision rule is proposed to determine if the given day is clear, discussed next.

A. Clear-Day Rule

For any given day, GHI and clear-sky GHI at a 30-min resolution are available from the NSRDB. The following rule is based on the heuristic that for clear days, variability of GHI and clear-sky GHI should be similar, whereas on other days, raw GHI will be more variable. Let $X(t)$ denote linearly interpolated NSRDB at time point t and $X_C(t)$ denote the clear-sky GHI. To quantify variability, we compute first-order differences as

$$\Delta X(t) = X(t) - X(t - 1) \tag{1}$$

$$\Delta X_C(t) = X_C(t) - X_C(t - 1) \tag{2}$$

and consider the quantity

$$\gamma = \max_t |\Delta X(t) - \Delta X_C(t)| \tag{3}$$

where the maximum is taken over a particular day. If this value is smaller than a given tolerance, we classify that day as a clear day; otherwise, it is non-clear. Fig. 2 shows histograms of γ values for each of the SURFRAD stations based on the year of 2013. For each station, the empirical distribution is concentrated at zero with a few values greater than 0.1; thus, we use $\gamma = 0.1$ as the cutoff for the decision rule. The high frequency of values near zero is indicative of clear days with other values indicating days of more complicated atmospheric conditions.

B. Non-Gaussian Mixture Model

Because the *in situ* GHI is theoretically consistent with ground measurements, the downscaling model is log-additive with an intercept of zero and a slope of one. The log-additive model contributes to reducing errors at the transition points between sunrise and sunset. Let $Y(t)$ be the *in situ* measurements from ground data, and $X(t)$ be the linear interpolation of GHI from the NRSDB on $t \in \mathbb{R}$. The model is of the form

$$\log(Y(t)) = \log(X(t)) + \epsilon(t). \tag{4}$$

The log data are potentially subject to noise $\epsilon(t)$, representing small-scale variability and measurement error. We model this variation using the non-Gaussian mixture.

In general, we simulate the noise using

$$\epsilon(t) = L\boldsymbol{\omega} = \sum_{i=1}^{n} \ell_{ti}\omega_i \tag{5}$$

where $L = (\ell_{ij})$ is the Cholesky factor of the covariance matrix of $\boldsymbol{\epsilon} = (\epsilon(1), ..., \epsilon(n))^T$, ℓ_{ti} stands for the (t, i)th entry of L, and
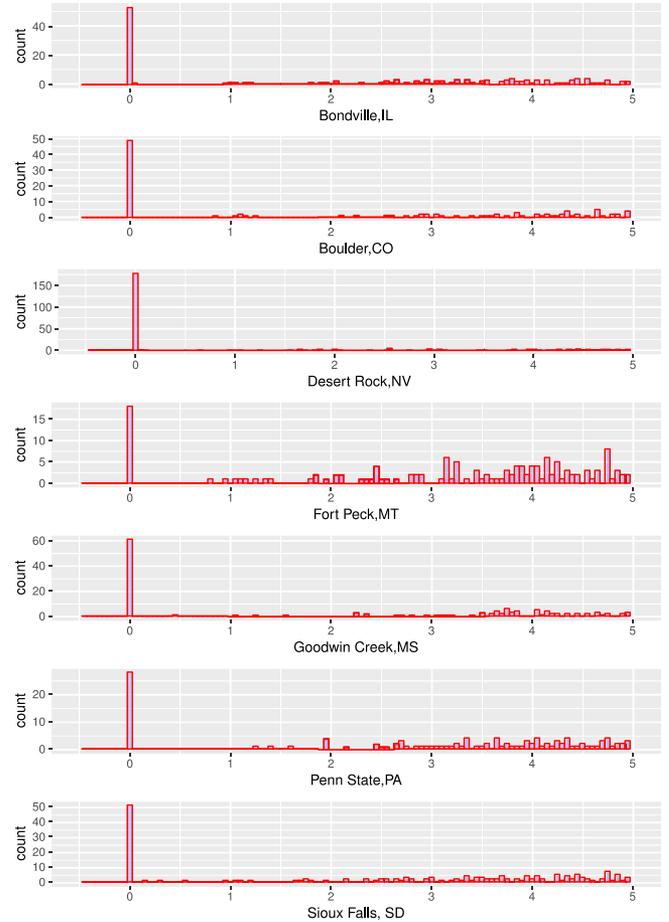

Fig. 2. Empirical distribution of γ for SURFRAD (γ is indexed on the x-axis).

$\boldsymbol{\omega} = (\omega_1, \ldots, \omega_n)^T$ is a vector of n independent random variables whose distribution will be specified later in this section. Note that $\boldsymbol{\omega} = L^{-1}\boldsymbol{\epsilon}$ are uncorrelated, which is referred to as the decorrelated residuals. Fig. 3 shows the empirical distribution of $\boldsymbol{\omega}$ at Eugene, OR, USA, for four sampled days in 2013. Note that $\boldsymbol{\omega}$ is concentrated at 0 with approximate support $[-2, 2]$. In this case, a mixture of a Beta distribution and a heavier tailed distribution is used to model $\boldsymbol{\omega}$. In particular, we propose

$$\omega_t = \theta\mu(t) + (1 - \theta)\nu(t) \tag{6}$$

where $\mu(t)$ and $\nu(t)$ are random variables with a centered and scaled Beta distribution and a t distribution, respectively. The value of $\theta \in [0, 1]$ is the weight parameter of the Beta distribution component.

After testing on days of 2013 at Oregon locations, we estimate the centered and scaled Beta distribution as $Beta(3.8, 4)$ and t distribution as $t(10)$. The expectation–maximization iterative algorithm is implemented to find θ for every single day.

C. Jump Process for Excursions Because of Scattering Events

Because of scattering events, we include jump processes for excursions. For example, the excursions beyond the theoretical clear-sky max can occur on days with clouds, e.g., January 1, as plotted in Fig. 1. On days with scattering events, each site
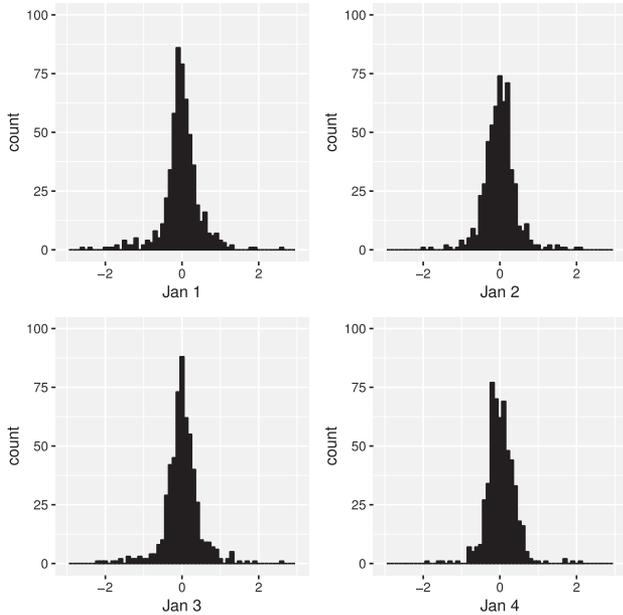
Fig. 3. Empirical distribution of $\hat{\omega}$ for Eugene, OR, USA, 2013.

experiences most excursions during the middle of the day, and each excursion is within a period of no more than 5 min. A jump process in which the timing and magnitudes are realistic based on the historical data not only allows us to interpolate the excursions at nearby unobserved sites, but provides a way to model the uncertainty of the interpolated excursions as well.

1) Noisy 30-min Time Interval: Let $X(t)$ denote the linearly interpolated NSRDB at time point t and $X_C(t)$ denote the linearly interpolated clear-sky GHI. To identify the timing for the jump process based only on the NSRDB, the first-order differences are computed as follows:

$$Z(t') = \sum_{t \in t'} \text{Var}(X(t)) \tag{7}$$

$$Z_C(t') = \sum_{t \in t'} \text{Var}(X_C(t)) \tag{8}$$

where t' is a 30-min time interval.

If $Z(t') > (1.2)^2 \times Z_C(t')$, then t' is considered a noisy 30-min time interval. Here, 1.2 is the maximum of the clearness index observed from the data used to train the model.

2) Cloud Cover Scenarios: Because clouds have remarkable implications for GHI, cloud cover scenarios are assumed to give more variability when certain cloud types occur at specific times of the day. There are 13 types of clouds in the NSRDB. The satellite images are taken from the University of Wisconsin, and cloud classification is performed using the PATMOS-X model, which divided the images into 12 classes [31]. Table III shows the cloud classifications.

To model realistic GHIs with respect to different noisy 30-min time intervals, the empirical distribution of excursions used in this work is conditioned both on cloud type and time of day. For any 30-min time interval between 9 A.M. and 3 P.M., days are selected with solar irradiance. For each cloud type and

TABLE III
CLOUD CLASSIFICATION

Cloud type number	Cloud type	Cloud grouping
0	Clear	Clear
1	Probably Clear	Cear
2	Fog	Water
3	Water	Water
4	Supercooled water	Water
5	Mixed	Water
6	Opaque ice	Ice
7	Cirrus	Ice
8	Overlapping	Ice
9	Overshooting	Ice
10	Unknown	Water
11	Dust	Clear
12	Smoke	Clear

interval, the proportion of those 30 samples greater than clear-sky GHI on these selected days is calculated separately. Thus, for each 30-min interval and each cloud type, the expected probability of excursions is calculated. The empirical distribution of excursions is shown in Table V, and the corresponding number of excursions for a given 30-min time interval and cloud type is shown in Table IV.

For the simulation, samples are taken as a random number of minutes that correspond to the empirical distribution of excursions for any noisy 30-min time interval with corresponding cloud type. At each excursion's sampled time point s, we have

$$\hat{Y}(s) \sim \text{Unif}(X(s), 1.2X(s)). \tag{9}$$

Overall, at an arbitrary time point t, if $\hat{Y}(t) > 1.2X_C(t)$, then

$$\hat{Y}(t) \sim \text{Unif}(X_C(t), 1.2X_C(t)). \tag{10}$$

Note that 1.2 comes from the data but could be tuned if other data suggested other maxima.

IV. RESULTS AND DISCUSSION

A. Initial Results

In the initial comparison, days were separated into clear, non-clear without excursions, and non-clear with excursions to be analyzed. Based on previous experience with γ values, $\gamma < 0.1$ are typically clear days. Thus, days with $\gamma < 0.1$ are classified as clear, and days with $\gamma \geq 0.1$ are classified as non-clear.

1) Non-Clear Days Without Excursions: On non-clear days without excursions, the model was found to slightly underestimate high-frequency irradiance variability. Fig. 4 shows a reliability plot with error bounds based on all validation locations for non-clear days without excursions during the year 2013. The x-axis represents the nominal coverage, whereas the y-axis is the corresponding empirical coverage for the stochastically downscaled estimates. The reliability plot compares empirical coverage against nominal coverage based on 1000 independent downscaled simulations. Good coverage properties at all nominal levels indicate a calibrated downscaling ensemble. As shown, the median of each boxplot is close to the identity

TABLE IV
NUMBER OF EXCURSIONS TRAINED BASED ON 2013 DATA

Cloud type	09:00–09:30	09:30–10:00	10:00–10:30	10:30–11:00	11:00–11:30	11:30–12:00
Clear	21	20	20	20	19	16
Water	3	3	4	4	4	4
Ice	1	1	1	0	2	1
Cloud type	12:00–12:30	12:30–13:00	13:00–13:30	13:30–14:00	14:00–14:30	14:30–15:00
Clear	10	6	4	3	3	2
Water	5	4	3	4	3	3
Ice	2	2	1	2	2	1

TABLE V
EMPIRICAL PROBABILITIES OF EXCURSIONS TRAINED BASED ON 2013 DATA

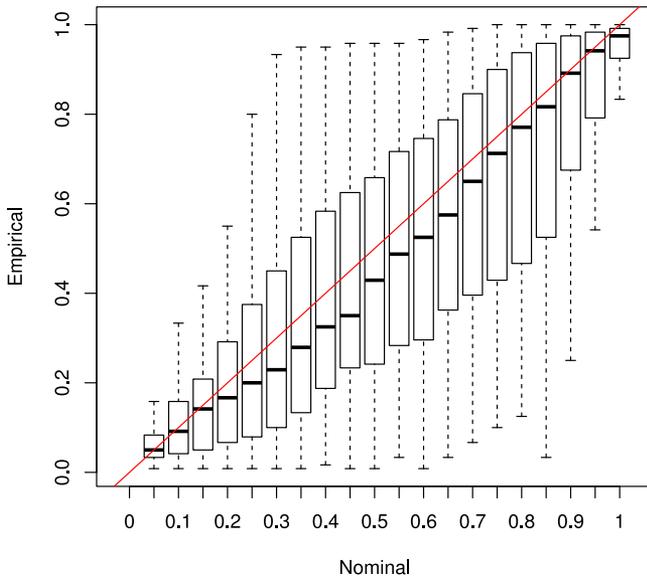| Cloud type	09:00–09:30	09:30–10:00	10:00–10:30	10:30–11:00	11:00–11:30	11:30–12:00
Clear	0.698	0.672	0.659	0.653	0.626	0.541
Water	0.108	0.112	0.118	0.125	0.148	0.132
Ice	0.026	0.021	0.020	0.011	0.058	0.035
Cloud type	12:00–12:30	12:30–13:00	13:00–13:30	13:30–14:00	14:00–14:30	14:30–15:00
Clear	0.326	0.202	0.136	0.114	0.107	0.075
Water	0.164	0.134	0.116	0.138	0.116	0.097
Ice	0.073	0.071	0.040	0.058	0.055	0.051

Fig. 4. Reliability plot based on all validation locations for non-clear days without excursions during the year 2013.

line, indicating accurate coverage; however, the median value is systematically under the identity line, which yields underdispersion. The variability indicated by the boxplot suggests that individual realizations tend to exhibit empirical coverage within ±20% of nominal in the worst case. On this type of day, although the model captures the underlying trends from the NSRDB data, it underestimates some of the high-frequency up and down ramps seen in the ground data. Overall, the model

for non-clear days without excursions exhibit good coverage probabilities.

2) Non-Clear Days With Excursions: Excursions occur when a scattering event happens. On non-clear days with excursions, GHI tends to have high-frequency irradiance variability. Besides maintaining the basic trends, a jump process is a pivotal factor to capture the spikes based on the cloud type and noisy 30-min time intervals. Fig. 5 contains the reliability plot with error bounds based on all validation locations for non-clear days with excursions during the year 2013. In Fig. 5, the median for each boxplot is very close to the identity line, indicating that the algorithm works well for non-clear days with excursions. The variability indicated by the boxplot suggests that individual realizations tend to exhibit empirical coverage within ±15% of nominal values.

To visualize how the model works for days with scattering events, Fig. 6 shows simulations along with clear-sky GHI and *in situ* measurements. In Fig. 6, the simulations are relatively reasonable compared to the ground measurements. There will still be excursions the algorithm will not capture—for example, the spikes on January 15. However, the proposed stochastic model is not expected to capture every scattering event, but rather the distribution of the downscaled ensembles should be accurate in both the magnitude and frequency of excursions.

B. Variability Analysis

Because of the method used to create the NSRDB, the satellite-derived high-frequency irradiance samples are not expected to match the ground-measured irradiances exactly. Specifically, the timing of clouds could not match between
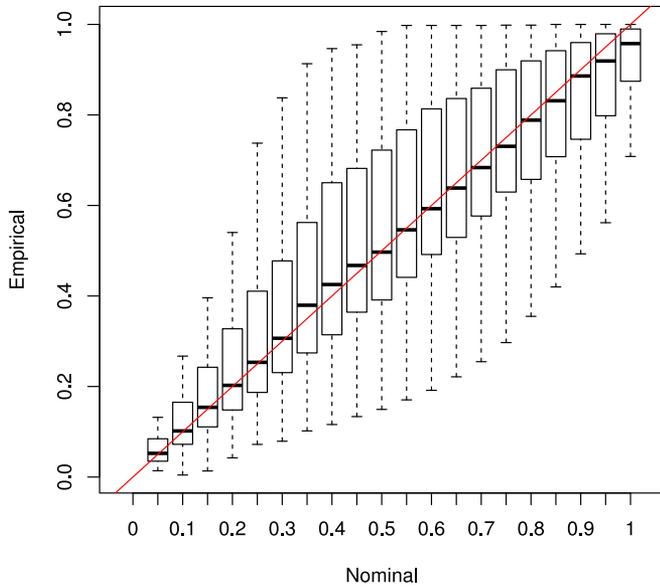
Fig. 5. Reliability plot based on all validation locations for non-clear days with excursions during the year 2013.
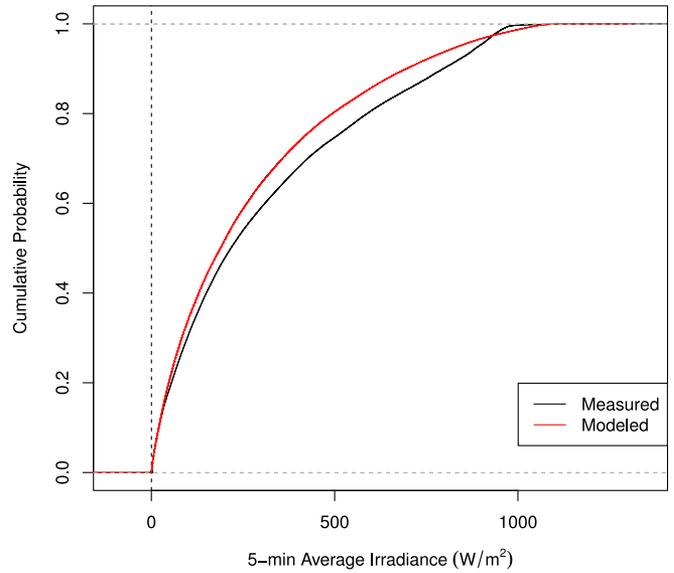

Fig. 7. Frequency distributions for mean 5-min irradiance average over all validation locations' simulated and *in situ* data in 2013.
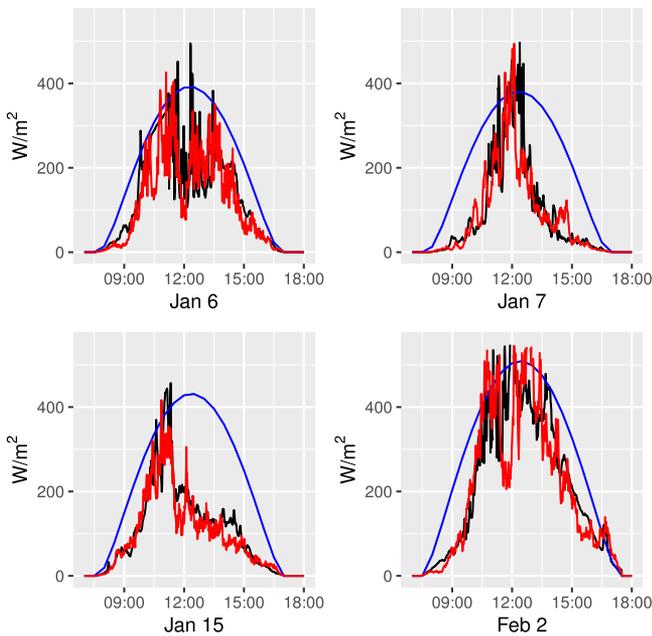

Fig. 6. Simulation (red), linear interpolated MaxGHI (blue), and *in situ* data (black) on non-clear days with excursions during the year 2013 for Eugene, OR, USA.

Fig. 8. Distribution function of 1-min ramp rates at all validation locations for 2013. The x-axis is the ramp magnitude, and the y-axis is the ramp probability.

satellite-downscaled and ground-measured irradiance variability. Instead, it is vital that the algorithm captures the overall irradiance variability statistics. Because the variability samples are most useful to understand the relative impact of solar variability on electric grid operations, comparison metrics that evaluate variability during different periods, such as 5 min, are necessary.

Fig. 7 shows the frequency distribution for 5-min average irradiance across all validation locations. The average irradiance is an aggregate statistic among all times and locations. The correlation between the simulated and measured averages is
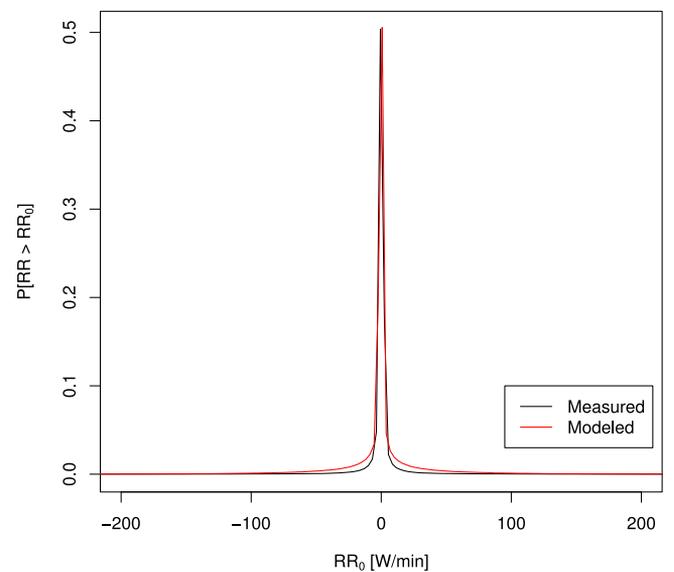
$R^2 = 0.925$, indicating that our method adequately captures first-moment statistics of actual 5-min aggregated irradiance.

Another critical aspect to accurately capture is the ramp rate, i.e., the change in output compared to the clear-sky estimation over a given timescale. Fig. 8 compares the 1-min ramp rate distribution between the synthetic data in all validation locations with the *in situ* ones. Our model estimates a higher than measured probability of a ramp between -50 and 50 W/min. Compared with the measured data, the modeled ramp rate distribution during 1-min time steps shows a strong correlation ($R^2 = 0.991$). Overall, the proposed approach does an adequate job of capturing ramps at different magnitudes.
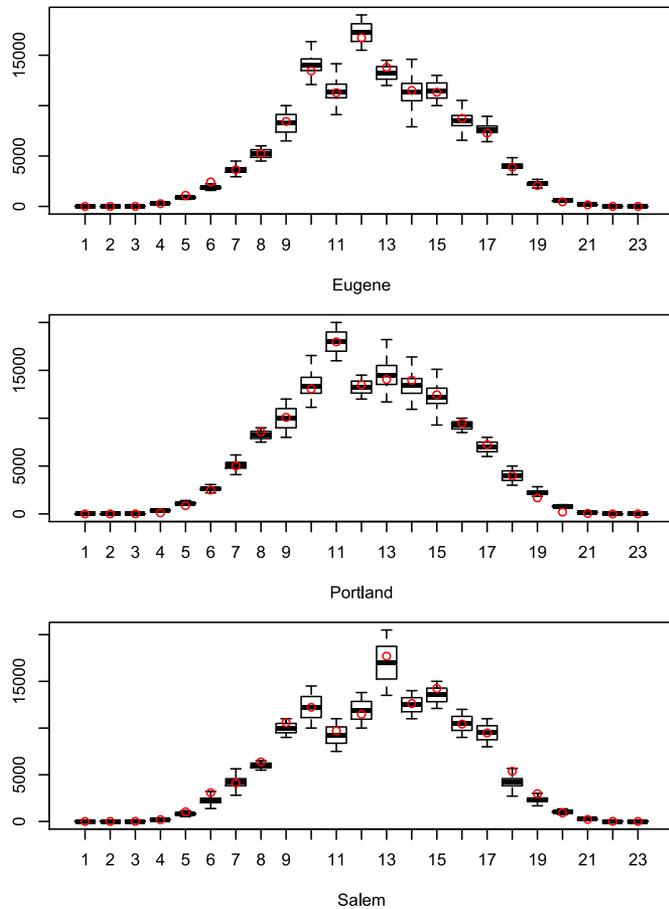
Fig. 9. Boxplots of 30-min variability estimates and observed 30-min variances (red circles) based on data from January, 2013 for the Oregon locations. The x-axis unit denotes the hour of the day.

Fig. 9 illustrates 30-minute variance estimates in January 2013 for the Oregon locations along with the corresponding observed variability. The uncertainty bounds for these 30-min variance estimates are based on 1000 simulations. The observations are mostly within the interquartile range, which are the 25% and 75% quantiles over the 1000 ensembles of empirical variances, which indicates that the model captures changing variability during short time frames.

V. CONCLUSION AND FUTURE WORK

The proposed stochastic model aims to downscale data products such as the NSRDB to a higher temporal frequency. The statistical model varies with the time of day and cloud type to capture excursions during daylight hours. We have validated the model at various locations based on a comprehensive set of statistical metrics on both non-clear days with excursions and without excursions. Our validation results suggest that the downscaled ensembles exhibit good coverage properties at most nominal levels, indicating a calibrated model. Moreover, crucial variability properties are maintained, and difficult statistics such as ramp rate distributions and frequency distribution of short period averages are well replicated by the model.

Future work might focus on temporally downscaling to an even finer time resolution, which requires high-frequency observational data for training as well. Because our method is still point level, another direction is to generalize this framework to allow for spatially correlated simulations and especially coherence between neighboring locations. Along this line, another future route is to determine how, without direct *in situ* data, high-frequency variability characteristics change throughout space and time.

REFERENCES

[1] Renewable Global Status Report, 2016.
[2] R. Shah, N. Mithulananthan, R. C. Bansal, and V. K. Ramachandaramurthy, "A review of key power system stability challenges for large-scale PV integration," *Renew. Sustain. Energy Rev.*, vol. 41, pp. 1423–1436, 2015.
[3] M. J. Reno, J. Debover, and B. Mather, "Motivation and requirements for quasi-static time-series (QSTS) for distribution systems," in *Proc. IEEE Power Energy Soc. Gen. Meeting*, 2017, pp. 1–5.
[4] M. Lave, J. Quiroz, M. J. Reno, and R. J. Broderick, "High temporal resolution load variability compared to PV variability," in *Proc. IEEE 44th Photovolt. Spec. Conf.*, 2017, pp. 1–6.
[5] B. Mather *et al.*, "NREL/SCE high penetration PV integration project: FY13 annual report," Nat. Renew. Energy Lab., Golden, CO, USA, Tech. Rep. NREL/TP-5D00-61269, 2014.
[6] H. Yang, C. Huang, Y. Huang, and Y. Pai, "A weather-based hybrid method for 1-day ahead hourly forecasting of PV power output," *IEEE Trans. Sustain. Energy*, vol. 5, no. 3, pp. 917–926, Jul. 2014.
[7] D. Yang *et al.*, "Solar irradiance forecasting using spatial-temporal covariance structure and time-forward kriging," *Renew. Energy*, vol. 60, pp. 235–245, 2013.
[8] R. Schmalensee, "The future of solar energy: A personal assessment," *Energy Econ.*, vol. 52, pp. S142–S148, 2015.
[9] R. Huang, T. Huang, R. Gadh, and N. Li, "Solar generation prediction using the ARMA model in laboratory-level micro-grid," in *Proc. IEEE 3rd Int. Conf. Smart Grid Commun.*, 2012, pp. 528–533.
[10] J. Boland, M. Korolkiewicz, M. Agrawal, and J. Huang, "Forecasting solar radiation on short time scales using a coupled autoregressive and dynamical system (CARDS) model," *Sol. Energy*, vol. 87, pp. 136–149, 2013.
[11] G. Reikardf, "Predicting solar radiation at high resolutions: A comparison of time series forecasts," *Sol. Energy*, vol. 83, pp. 342–349, 2009.
[12] C. Glasbey, R. Graham, and A. Hunter, "Spatio-temporal variability of solar energy across a region: A statistical modeling approach," *Sol. Energy*, vol. 70, pp. 373–381, 2001.
[13] J. Mubiru, "Predicting total solar irradiation values using artificial neural networks," *Renew. Energy*, vol. 33, pp. 2329–2332, 2008.
[14] Z. Wang, F. Wang, and S. Su, "Solar irradiance short-term prediction model based on BP neural network," *Sol. Energy*, vol. 12, pp. 488–494, 2011.
[15] K. A. Baharin, H. A. Bahman, M. Y. Hassan, and C. K. Gan, "Hourly irradiance forecasting in Malaysia using support vector machine," in *Proc. IEEE Conf. Energy Convers.*, 2014, pp. 185–190.
[16] F. Meizi, T, Touati, A. Same, and L. Oukhellou, "Hourly solar irradiance forecasting based on machine learning models," in *Proc. 15th Int. Conf. Mach. Learn. Appl.*, 2016, pp. 441–446.
[17] C. W. Chow, B. Urquhart, M. Lave, A. Dominguez, J. Kleissl, and J. Shields, "Intra-hour forecasting with a total sky imager at the UC San Diego solar energy tested," *Sol. Energy*, vol. 85, pp. 2881–2893, 2011.
[18] E. Lorenz, J. Hurka, D. Heinemann, and H. G. Beyer, "Irradiance forecasting the power prediction of grid-connected photovoltaic systems," *IEEE J. Sel. Topics Appl. Earth Observ. Remote Sens.*, vol. 2, no. 1, pp. 2–10, Mar. 2009.
[19] M. Diagne, D. Mathieu, J. Boland, N.Schmutz, and P. Lauret, "Post-processing of solar irradiance forecasts from WRF model at Reunion Island," *Sol. Energy*, vol. 105, pp. 99–108, 2014.
[20] A. W. Aryaputera, H. Verbois, and W. M. Walsh, "Probabilistic accumulated irradiance forecast for Singapore using ensemble techniques," in *Proc. IEEE 43rd Photovolt. Spec. Conf.*, 2016, pp. 1113–1118.

[21] M. Hummon, E. Ibanez, G. Brinkman, and D. Lew, "Sub-hourly solar data for power system modeling from static spatial variability analysis," in *Proc. 2nd Int. Workshop Integr. Sol. Power Power Syst.*, Lisbon, Portugal, 2012, pp. 1–7.

[22] M. Lave, J. Kleissl, and J. S. Stein, "A wavelet-based variability model (WVM) for solar PV power plants," *IEEE Trans. Sustain. Energy*, vol. 4, no. 2, pp. 501–509, Apr. 2013.

[23] J. M. Bright, C. Smith, P. G. Taylor, and R. Crook, "Stochastic generation of synthetic minutely irradiance time series derived from mean hourly weather observation data," *Sol. Energy*, vol. 115, pp. 229–242, 2015.

[24] J. M. Bright, O. Babacan, J. Kleissl, P. G. Taylor, and R. Crook, "A synthetic spatially decorrelating solar irradiance generator and application to a LV grid model with high PV penetration," *Sol. Energy*, vol. 147, pp. 83–98, 2017.

[25] T. E. Hoff and R. Perez, "Quantifying PV power output variability," *Sol. Energy*, vol. 84, pp. 1782–1793, 2010.

[26] M. Lave, J. Kleissl, and E. Arias-Castro, "High frequency irradiance fluctuations and geographic smoothing," *Sol. Energy*, vol. 86, pp. 2190–2199, 2012.

[27] M. J. Perez and V. M. Fthenakis, "On the spatial decorrelation of stochastic solar resource variability at long timescales," *Sol. Energy*, vol. 117, pp. 46–58, 2015.

[28] C. M. Fernández-Peruchena, M. Blanco, M. Gastón, and A. Bernardos, "Increasing the temporal resolution of direct normal solar irradiance series in different climatic zones," *Sol. Energy*, vol. 115, pp. 255–263, 2015.

[29] C. M. Fernández-Peruchena and M. Gastón, "A simple and efficient procedure for increasing the temporal resolution of global horizontal solar irradiance series," *Renew. Energy*, vol. 86, pp. 375–383, 2016.

[30] C. F. Peruchena, M. Larrañeta, M. Blanco, and A. Bernardos, "High frequency generation of coupled GHI and DNI based on clustered dynamic paths," *Sol. Energy*, vol. 159, pp. 453–457, 2018.

[31] M. Sendupta, Y. Xie, A. Lopez, A. Habte, G. Maclaurin, and J. Shelby, "The National Solar Radiation Data Base (NSRDB)," *Renew. Sustain. Energy Rev.*, vol. 40, pp. 51–60, 2018.

[32] C. A. Gueymard, "REST2: High-performance solar radiation model for cloudless-sky irradiance illuminance, and photosynthetically active radiation—Validation with a benchmark dataset," *Sol. Energy*, vol. 82, pp. 272–285, 2013.

[33] F. Vignola and R. Perez, "Solar Resource GIS Data Base for the Pacific Northwest using satellite data—Final report," Univ. Oregon Solar Radiation Monit. Lab., Eugene, OR, USA, Tech. Rep. DE-PS36-0036-00GO10499, 2004.

[34] J. A. Augustine, J. J. DeLuisi, and C. N. Long, "SURFRAD—A national surface radiation budget network for atmospheric research," *Bull. Amer. Meteorol. Soc.*, vol. 81, pp. 2341–2357, 2000.

[35] M. J. Reno and C. W. Hansen, "Identification of periods of clear sky irradiance in time series of GHI measurements," *Renew. Energy*, vol. 90, pp. 520–531, 2016.

Authors' photographs and biographies not available at the time of publication.